Numerical Suite for Cathodeless Plasma Thrusters

M. Magarotto[a,*], S. Di Fede[b], N. Souhair[c], S. Andrews[c], F. Ponti[c]

[a] *University of Padova, Department of Industrial Engineering (DII), via Gradenigo 6/a,
35131, Padova, Italy*
[b] *University of Padova, Center of Studies and Activities for Space "G. Colombo" (CISAS),
via Venezia 15, 35131, Padova, Italy*
[c] *University of Bologna, Department of Industrial Engineering (DIN), Via Fontanelle 40,
47122, Forlì, Italy*

Abstract

This work focuses on a numerical suite targeted at cathodeless plasma thrusters. A Global Model is used for preliminary estimation of the propulsive performance. In the plasma source, the code 3D-VIRTUS solves self-consistently plasma transport with a fluid approach, including the electromagnetic wave propagation. Starfish and SPIS are used to handle the magnetic nozzle region via a fully kinetic Particle-in-Cell (PIC) model. Starfish solves the plasma dynamics in a two-dimensional axisymmetric domain and has been coupled to 3D-VIRTUS in order to estimate the propulsive performance. SPIS is a three-dimensional PIC code that has been used to simulate the mutual interactions between the satellite surfaces, the propulsion system plumes and the environmental plasma. Results have been benchmarked against thrust measurements performed on a low-power (50 W range) Helicon Plasma Thruster.

Keywords: Electric Propulsion, Helicon Plasma Thruster, Plasma Simulation, Fluid Simulation, Particle-in-Cell

*mirko.magarotto@unipd.it

List of Symbols

n_I	density of the species I
n_e	electron density
T_e	electron temperature
R_{chem}^I	species I source/sink term due to plasma reactions
R_{wall}^I	species I source/sink term due to wall losses
R_{ex}^I	species I source/sink term due to particles outflow
R_{in}^I	species I source/sink term due to particles inflow
P_{RF}	electric power coupled to the plasma
P_{chem}	power source/sink term due to plasma reactions
P_{wall}	power source/sink term due to wall losses
P_{ex}	power source/sink term due to particles outflow
e, Xe$^+$, Xe	electrons, ionized and neutral xenon
K_{IJ}	rate constant for the inelastic transition from species I to species J
ΔU	energy difference between species I to species J
K_{II}	rate constant for the elastic collision between species I and electrons
m_I	mass of species I
m_e	electron mass
S_{wall}^I	equivalent surface area of species I for wall losses
S_{ex}^I	equivalent surface area of species I for particles outflow
Γ_{wall}^I	particle flux of species I related to wall losses
Γ_{ex}^I	particle flux of species I related to particles outflow
V	source volume
u_B	Bohm speed
$\beta,\ h_L,\ h_R,\ h_c$	semi-empirical coefficients related to non-uniform plasma density
A_L	cross section area of the cylindrical plasma source
A_R	lateral surface area of the cylindrical plasma source
A_c	equivalent area influenced by magnetic cusps
N_c	number of cusps
$r_i,\ r_e$	ion and electron cyclotron radius

u_{th}	thermal speed
$\dot{m}_0$	mass flow rate
M_{det}	magnetic Mach number at detachment
q	elementary charge
F_p	thrust associated to plasma expansion
p_I	pressure of the species I
F_g	thrust associated to neutral gas expansion
F	total thrust
I_{sp}	specific impulse
g_0	standard gravitational acceleration
n_ε	electron energy density
ϕ	plasma potential
ρ	charge density
ε_0	permittivity of vacuum
$\mathbf{\Gamma}^I$	particles flux of species I
$\mathbf{\Gamma}^e$	electrons flux
$\mathbf{\Gamma}^\varepsilon$	electron energy flux
$\bar{\bar{\mu}}_I$	mobility of the species I
$\bar{\bar{D}}_I$	diffusion coefficient of the species I
$\mathbf{u}_0$	convection speed
$\bar{\bar{\mu}}_e$	electrons mobility
μ_e^{DC}	scalar electrons mobility
$\chi,\ \chi_x,\ \chi_y,\ \chi_z$	normalization parameters of the magnetostatic field
α	anomalous transport coefficient
$\bar{\bar{\mu}}_\varepsilon$	mobility of the electron energy
$\bar{\bar{D}}_\varepsilon$	diffusion coefficient of the electron energy
$\mathbf{J}_{RF}$	current density induced by the RF antenna on the plasma
$\mathbf{E}_{RF}$	electric field induced by the RF antenna on the plasma
$\mathbf{r}$	particles position
$\mathbf{v}$	particles speed
Δt	time step

$\mathbf{E}$	electrostatic field
$\mathbf{B}$	magnetostatic field
ϕ_∞	plasma potential at an infinite distance from the thruster
E_{tot}	total energy of the electrons
C	equivalent capacitance of the thruster
r_b	perpendicular distance between the centre of the thruster outlet and the boundary
I_{iB}, I_{eB}	total ion and electron current at the external boundary
I_{i*}, I_{e*}	total ion and electron current emitted at the thruster outlet
n_{i0}, n_{e0}	ion and electron density at the thruster outlet
$\dot{m}_{i*}$	ion mass flow rate emitted at the thruster outlet
K	proportionality constant to control the emitted electron current
I_{e0}	net electron current at the thruster outlet
$\hat{\mathbf{z}}$	unit vector aligned with the axis of the thruster
$\hat{\mathbf{k}}$	unit vector perpendicular to the boundaries
S_B	surface of the external boundary
Δx	mesh spacing
λ_D	Debye length
γ	scaling coefficient of the vacuum permittivity
k_B	Boltzmann constant
$\tilde{\varepsilon}_0$	scaled vacuum permittivity
$\Delta \tilde{t}_{pe}$	time step to resolve the scaled plasma frequency
Δt_{ce}	time step to resolve the electron gyro-frequency
Δt_{CFL}	time step to resolve the Courant–Friedrichs–Lewy condition
$\tilde{\omega}_{pe}$	scaled plasma frequency
ω_{ce}	electron cyclotron frequency
ν_B	equivalent Bohm collision frequency
L	plasma source length
D	plasma source diameter
B_0	magnetic field at the thruster outlet
L_A	antenna length
D_A	antenna diameter

w_A	antenna wire width
Pw	input power
η_A	antenna efficiency
r, z	radial and axial coordinates
J_A	current density profile on the antenna
D_p	displacement electric field in the plasma
Z	antenna impedance
H_c, L_c, W_c	dimensions of the spacecraft in 3D PIC simulations
O^+	oxygen ions in the environmental plasma
x, y, z	cartesian coordinates in the 3D PIC simulations
$\mathbf{V}_{SC}$	spacecraft velocity
v_{O+}, v_{Xe+}	speed of O^+ and Xe^+ particles
n_{Xe+}	density of Xe^+ particles
N_{tetr}	number of tetrahedra of the plasma mesh (EM module)

1. Introduction

Over the last decade, the field of electric propulsion has seen considerable active research, even though mature technologies such as Gridded Ion Thrusters (GIT) and Hall Effect Thrusters (HET) are readily available on the market [1, 2]. Particular effort has been put into the development of cathodeless plasma thrusters due to multiple system-related advantages, such as the propellant flexibility associated to the absence of electrodes and the quasi-neutral plasma jet eliminating the need for a neutraliser. Helicon Plasma Thrusters (HPT) [3, 4] and Electron Cyclotron Resonance Thrusters (ECRT) [5] are among the most promising cathodeless technologies. In these devices, plasma is produced within a dielectric tube where the neutral gas propellant is injected. An antenna, operated in the Radio Frequency (RF) or microwave range, sustains the discharge, coupling Electromagnetic (EM) power to the plasma [6]. Magnets produce a magnetostatic field that has three main functions: (i) increasing the efficiency of the source by enhancing the plasma confinement [7], (ii) driving the power coupling between the antenna and the plasma [8], and (iii) improving the propulsive performance via the magnetic nozzle effect downstream of the thruster outlet [9]. As a result, the design of a cathodeless system is much simpler with respect to GITs and HETs, making this technology highly appealing for the SmallSat market [10, 11] or interplanetary missions [12].

However, cathodeless devices still require improvements. For example, HPTs currently present a moderate thruster efficiency, never measured above 20% [3, 13]. Therefore, it is necessary to gain a deep physical insight into both the plasma generation and acceleration mechanisms to improve the propulsive performance. The key physical phenomena that govern the plasma dynamics in the production stage (see Fig. 1) are the EM wave propagation [14], the plasma transport [15], and their mutual coupling [16]. Instead, acceleration and magnetic detachment phenomena [17], that take place downstream of the plasma source, dictate the acceleration stage (see Fig. 1). The latter is characterised by the formation of a plume where the plasma is more rarefied than in the pro-
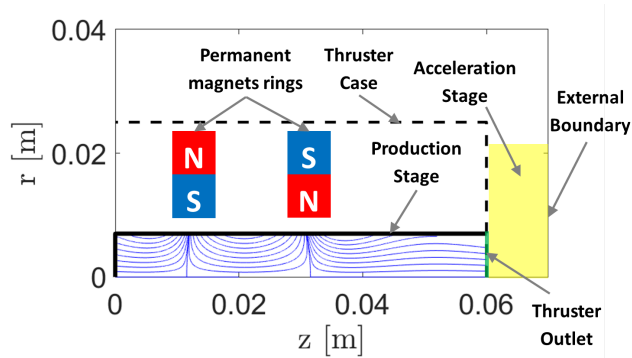
6

Figure 1: Schematic of a cathodeless plasma thruster. Magnetic field lines highlighted within the plasma source.

duction stage (density in the range 10^{16}-10^{18} m^{-3}) [18]. Particle collisions and the geometry of the applied magnetostatic field determine the plasma behaviour near to the thruster outlet [19]. Further downstream, the plasma expansion is driven by the thermal pressure and the ambipolar diffusion [19].

40   Given the complexity and the variety of the phenomena involved in the dynamics of a cathodeless plasma thruster, several theoretical and numerical strategies have been adopted to predict the propulsive performance. Three analytical models have been developed by Lafleur [20], Ahedo and Navarro-Cavallé [21], and Fruchtman et al. [22]. These tools are particularly useful in

45   the preliminary design of the thruster. Nonetheless, more advanced numerical instruments must be adopted for the optimisation process. Several numerical approaches have been pursued in the literature for modelling both the production stage and the acceleration stage. The most relevant are: fluid [23], kinetic [24], Particle-in-Cell (PIC) [25], and hybrid [26].

50   In this work, a numerical suite for cathodeless plasma thrusters is presented and its exploitation in a low-power (50 W range) case is discussed. A Global Model is first used for the preliminary estimation of propulsive performance [27, 28]. More advanced tools have then been developed to predict the plasma dynamics throughout the thruster. The 3D-VIRTUS code [16] solves, with a

55   fluid approach [29], the plasma transport within the production stage and the

7

Table 1: Plasma reactions considered.

Reaction	Formula	Reference
Elastic scattering	$Xe + e \longrightarrow Xe + e$	[32]
Ionisation	$Xe + e \longrightarrow Xe^+ + 2e$	[32]
Excitation	$Xe + e \longrightarrow Xe^* + e \longrightarrow Xe + e + h\nu$	[32]

EM wave propagation [14]. The fully kinetic PIC tools Starfish [30] and SPIS [31] have been customised in-house to simulate the plasma dynamics within the magnetic nozzle. Starfish, which handles two-dimensional (2D) axisymmetric domains, has been coupled to 3D-VIRTUS in order to estimate the propulsive performance. SPIS, a three-dimensional (3D) PIC, has been used to evaluate the mutual interactions between the propulsion system plume, the spacecraft surfaces, and the environmental plasma in a non-axisymmetric domain.

2. Methodology

2.1. Global Model

The main assumptions associated to the Global Model [27, 28] are: (i) cylindrical geometry of the plasma source, (ii) an axisymmetric magnetostatic field, (iii) presence of magnetic cusps in the source that can be simulated via a dedicated semi-empirical model [2], (iv) the paraxial approximation holds in the acceleration stage [20], and (v) in the acceleration stage plasma is frozen to the field lines up to the detachment. The dynamics of the source are solved according to the conservation of mass (Eq. 1) and electron energy (Eq. 2) equations

$$\frac{dn_I}{dt} = R^I_{chem} - R^I_{wall} - R^I_{ex} + R^I_{in} \tag{1}$$

$$\frac{d}{dt}\left(\frac{3}{2}n_e T_e\right) = P_{RF} - P_{chem} - P_{wall} - P_{ex} \tag{2}$$

where n_I is the number density of the species I. With this study focused on a xenon plasma, $I = e, i, g$ for electrons, ions (Xe^+), and ground state (Xe)

8

atoms respectively. T_e is the electron temperature in eV. For the species I, R_{chem}^I is the source/sink term associated to plasma reactions, R_{wall}^I to wall losses, R_{ex}^I to particles outflow, and R_{in}^I to particles inflow. P_{RF} is the power coupled to the plasma, along with P_{chem} is the source/sink term associated to plasma reactions, P_{wall} to wall losses, and P_{ex} to particles outflow. The plasma reactions considered are elastic scattering, ionisation and excitation (see Table 1), therefore the R_{chem}^I and P_{chem} terms read [32]

$$R_{chem}^I = \sum_J K_{JI} n_J n_e - \sum_J K_{IJ} n_I n_e \tag{3}$$

$$P_{chem} = \sum_I \sum_J K_{IJ} n_I n_e \Delta U_{IJ} + \sum_I K_{II} n_I n_e \frac{3m_e}{m_I} T_e \tag{4}$$

where K_{IJ} is the rate constant for the inelastic transitions from species I to species J, K_{II} is the rate constant for elastic collisions between species I and electrons, ΔU_{IJ} is the energy difference (in eV) between species I and species J, and m_e and m_I are the electron mass and the species I mass respectively [33]. Assuming the Bohm sheath criterion at the source walls, and a sonic thruster outlet [28], similar expressions hold for R_{wall}^I and R_{ex}^I

$$R_{wall}^I = \frac{S_{wall}^I}{V} \Gamma_{wall}^I \tag{5}$$

$$R_{ex}^I = \frac{S_{ex}^I}{V} \Gamma_{ex}^I \tag{6}$$

where V is the volume of the source, S^I is the equivalent surface area of the source, and Γ^I is the particle flux. For ions and electrons $\Gamma^e = \Gamma^i = n_e u_B$ where u_B is the Bohm speed [28].Considering the equivalent surface

$$S^e = S^i = \beta h_L A_L + h_R (A_R - A_c) + h_c A_c \tag{7}$$

where β, h_L, h_R, and h_c are semi-empirical coefficients that account for the non-uniform plasma density distribution within the source [28]. A_L is the cross sectional area, A_R the lateral surface area, and A_c the equivalent area influenced by magnetic cusps. The latter parameter reads [2] $A_c = 4\sqrt{r_e r_i} \pi D N_c$ where N_c is the number of magnetic cusps, D is the diameter of the source, and r_i

(r_e) is the ion (electron) gyroradius. For neutrals $R_{wall}^g = -R_{wall}^e$, assuming total recombination at the walls [29]. Instead, S_{ex}^g is equal to the physical thruster outlet area and, assuming the neutrals are in the free-molecular regime, $\Gamma^g = 1/4 n_g u_{th}$; u_{th} is the neutrals thermal speed [30]. From the Bohm sheath criterion, the energy terms read [28]

$$P_{wall} = R_{wall}^e \left(2 + \log \sqrt{\frac{m_i}{2\pi m_e}} \right) T_e \tag{8}$$

$$P_{ex} = R_{ex}^e \left(2 + \log \sqrt{\frac{m_i}{2\pi m_e}} \right) T_e \tag{9}$$

Regarding the gas inflow, only neutral species are assumed to be injected into the source

$$R_{ex}^g = \frac{\dot{m}_0}{V m_g} \tag{10}$$

where $\dot{m}_0$ is the propellant mass flow rate.

The thrust F is then computed according to the model presented in [20]. The contribution from the plasma F_p is

$$F_p = \frac{M_{det}^2 + 1}{M_{det}} q n_e T_e S_{ex}^e \tag{11}$$

where q is the elementary charge, and M_{det} is the magnetic Mach number (u/u_B) at the detachment point. M_{det} is computed according to the detachment criterion prescribed in [20]. The contribution to the thrust due to neutral gas expansion is

$$F_g = p_g S_{ex}^g \tag{12}$$

where p_g is the neutral pressure. Total thrust and specific impulse, where g_0 is the standard gravitational acceleration, then read

$$F = F_p + F_g \tag{13}$$

$$I_{sp} = \frac{F}{g_0 \dot{m}_0} \tag{14}$$

2.2. Source Solver

The plasma source is handled with the 3D-VIRTUS code [16]. Plasma transport and EM wave propagation are solved self-consistently by means of two

distinct modules, namely the fluid module and the EM module, which run iter-
atively until convergence. In the former, the plasma transport is solved in a 2D
domain while the latter uses a 3D domain [14].

The species considered in the fluid module are electrons, ions (Xe^+) and
neutrals (Xe); all of them have been assumed to have a Maxwellian distribu-
tion function. Notably, this hypothesis is justified for HPTs even tough two-
temperature electron distribution functions have been observed in Helicon ex-
periments [3, 34]. In fact, deviations from Maxwellian are not expected to pro-
duced major effects on the electron dynamics in typical Helicon discharges [35].
Assuming a Maxwellian distribution for ions is also not expected to affect the
results of the simulation, apart from in the lower hybrid frequency range [36].
The governing equations of the fluid module are continuity, energy and Poisson's

$$\frac{\partial n_I}{\partial t} + \nabla \cdot \mathbf{\Gamma}^I = R^I_{chem} \tag{15}$$

$$\frac{\partial n_\varepsilon}{\partial t} + \nabla \cdot \mathbf{\Gamma}^\varepsilon - \nabla\phi \cdot \mathbf{\Gamma}^e = P_{RF} - P_{chem} \tag{16}$$

$$\varepsilon_0 \nabla^2 \phi = -\rho \tag{17}$$

where $n_\varepsilon = 3/2 n_e T_e$ is the energy density, ϕ is the plasma potential, $\rho = q(n_i - n_e)$ is the charge density, and ε_0 is the permittivity of vacuum. Formally,
the terms R^I_{chem} and P_{chem} are reported in Eq. 5 and Eq. 8, but in 3D-VIRTUS
they are scalar fields which depend on position. Reactions considered are listed
in Table 1. $\mathbf{\Gamma}^I$ is the flux of the species I that, according to the drift diffusion
approximation of the momentum equation [16], reads

$$\mathbf{\Gamma}^I = \pm\bar{\bar{\mu}}_I n_I \nabla\phi - \bar{\bar{D}}_I \nabla n_I + \mathbf{u}_0 n_I \tag{18}$$

where $\bar{\bar{\mu}}_I$ and $\bar{\bar{D}}_I$ are the mobility and the diffusion coefficient of the species I,
whose values are prescribed in [29]. Specifically, the anisotropy of the electron
transport across the magnetic field lines is accounted via the following expression
of the electron mobility [29]

$$\bar{\bar{\mu}}_e = \frac{\mu_e^{DC}}{\left(1+\alpha\chi\right)^2 + \chi^2} \left[\begin{pmatrix} 1+\alpha\chi & -\chi_z & \chi_y \\ \chi_z & 1+\alpha\chi & -\chi_x \\ -\chi_y & \chi_x & 1+\alpha\chi \end{pmatrix} + \right.$$

11

$$+\left(1+\alpha/\chi+\alpha^2\right)\left.\begin{pmatrix} \chi_x^2 & \chi_x\chi_y & \chi_x\chi_z \\ \chi_y\chi_x & \chi_y^2 & \chi_y\chi_z \\ \chi_z\chi_x & \chi_z\chi_y & \chi_z^2 \end{pmatrix}\right] \tag{19}$$

where μ_e^{DC} is the scalar electron mobility [29], $\chi = \mu_e^{DC}B$, $\mathbf{B} = (B_x, B_y, B_z)$ is the magnetic field vector, $\chi_k = \mu_e^{DC}B_k$ ($k = x,\ y,\ z$), and α is the anomalous transport coefficient assumed equal to 10^{-2} [37, 38, 39]. The parameter $\mathbf{u}_0$ is the convection speed, assumed aligned with the thruster axis and equal in modulus to $1/4u_{th}$ [7]. It is worth noting that the drift diffusion approximation of the momentum equation holds when the pressure within the plasma source is within 10^{-2}-10^{-3} mbar [16], as in the case at hand (see Section 3). $\mathbf{\Gamma}^\varepsilon$ is the energy flux that reads

$$\mathbf{\Gamma}^\varepsilon = \bar{\bar{\mu}}_\varepsilon n_\varepsilon \nabla\phi - \bar{\bar{D}}_\varepsilon \nabla n_\varepsilon + \mathbf{u}_0 n_\varepsilon \tag{20}$$

where $\bar{\bar{\mu}}_\varepsilon$ and $\bar{\bar{D}}_\varepsilon$ are derived according to the Einstein relations [29]. The power deposition profile is computed via the EM module and it reads [16]

$$P_{RF} = \frac{1}{2}q\mathrm{Re}\left(\mathbf{J}_{RF}^* \cdot \mathbf{E}_{RF}\right) \tag{21}$$

where $\mathbf{J}_{RF}$ and $\mathbf{E}_{RF}$ are the complex values of the current density and the electric field induced by the RF antenna onto the plasma. It is worth highlighting that the solution of the EM wave propagation, and in turn of P_{RF}, accounts for the self-consistent interactions between the plasma and each metallic component of the system (e.g., antenna and magnets).

A Robin type boundary condition is imposed to the electron continuity and energy to enforce the Bohm sheath criterion [16]. A zero-gradient Neumann type condition is imposed to the continuity of ions (see the Appendix for further details on this assumption). At the walls, a Neumann condition is imposed to the continuity of the neutrals in order to enforce the recombination of the charged species [29]. At the thruster outlet, the neutral density gradient is assumed null [7]. Finally, a Neumann type boundary condition is imposed to the Poisson's equation to enforce the equality between ion and electron fluxes at the dielectric walls [29]. The thruster outlet is grounded to the reference potential of $\phi_0 = 0$ [16, 30].

12

2.3. Plume Solver

The plasma expansion in the plume has been simulated with two different fully kinetic PIC solvers, namely Starfish [30] and SPIS [31]. The former handles axisymmetric domains while the particle speed is solved in 3D; the latter is fully 3D. Starfish has also been coupled to 3D-VIRTUS in order to solve the plasma dynamics in the overall thruster and, in turn, to estimate the propulsive performance (see Section 2.4). SPIS has instead been used to predict the mutual interaction between the plasma plume, the spacecraft, and the environmental plasma in a non-axisymmetric domain.

The dynamics of ions (Xe^+), electrons and neutrals (Xe) are all tracked via macroparticles. Particle velocity is updated according to the discrete equation of motion [40]

$$\frac{\mathbf{v}^{t+1/2} - \mathbf{v}^{t-1/2}}{\Delta t} = \frac{q_I}{m_I}\left(\mathbf{E}^t + \frac{\mathbf{v}^{t+1/2} + \mathbf{v}^{t-1/2}}{2} \times \mathbf{B}\right) \tag{22}$$

$$\frac{\mathbf{r}^{t+1} - \mathbf{r}^t}{\Delta t} = \mathbf{v}^{t+1/2} \tag{23}$$

where $\mathbf{r}^t$ and $\mathbf{v}^t$ are the particle position and velocity at time-step t, Δt is the time step, $\mathbf{E}$ is the electric field and $\mathbf{B}$ the magnetic field. This is solved with the conventional Boris scheme [41]. Since the RF power deposition in the acceleration stage is assumed negligible [31], the EM fields in the plasma are calculated via the electrostatic Poisson's equation. Therefore, $\mathbf{B}$ is the background magnetostatic field and $\mathbf{E} = -\nabla\phi$ where

$$\varepsilon_0 \nabla^2 \phi = -\rho \tag{24}$$

with ρ computed from particle positions via a second-order deposition scheme [30].

Based on an expected mean free path analysis compared to the scale of the simulation domain [30], six different collisional processes are considered: electron-electron Coulomb scattering [42], electron-ion Coulomb scattering [42], electron-neutral elastic scattering [43], ion-neutral elastic scattering [44] and charge exchange [45], along with neutral-neutral elastic scattering [46]. Inelastic ionisation and excitation collisions are negligible at the electron temperatures

13

considered in this work [27]. Anomalous electron transport is included using an equivalent Bohm collision frequency $\nu_B = \alpha\omega_{ce}$ [47], where $\omega_{ce} = qB/m_e$ is the electron cyclotron frequency and $\alpha = 10^{-2}$ was taken based on the observations of references [37, 38, 39].

Regarding boundary conditions (see Fig. 1), Eq. 25 holds for the Poisson's equation

$$\begin{cases} \phi = 0 & \text{Thruster outlet} \\ d\phi/dk = 0 & \text{Thruster case} \\ d\phi/dk + (\phi - \phi_\infty)/r_b = 0 & \text{External boundary} \end{cases} \tag{25}$$

where k is the direction normal to the external boundary, r_b is the perpendicular distance between the centre of the thruster outlet and the boundary, and ϕ_∞ is the potential at infinity. This condition imposed at the external boundary derives from the assumption that $\phi \propto 1/r$ for $r \longrightarrow \infty$ [30]. The condition on the thruster case assumes it is a perfect dielectric. Regarding kinetic boundary conditions, ions and electrons that reach the thruster outlet or the thruster case are removed from the simulation domain [31]. The same condition holds for the ions at the external boundary [31], where an energy-based criterion is used to account for the electrons "trapped" by the potential drop across the plume [30]. The total energy of each electron that reaches the external boundary is computed according to Eq. 26

$$E_{tot} = \frac{1}{2}m_e|\mathbf{v}_e|^2 - q\phi \tag{26}$$

If $|E_{tot}| > |q\phi_\infty|$ the electron is absorbed, since its energy is high enough to escape to the infinity. Else, if $|E_{tot}| < |q\phi_\infty|$ the particle is considered "trapped" and it is subject to a complete reflection $\mathbf{v}_e = -\mathbf{v}_e$. A control loop has then been implemented to enforce current-free and quasi-neutral conditions at the thruster outlet [31]. The value of the potential at infinity is updated according to Eq. 27.

$$\phi_\infty^{t+1} = \phi_\infty^t + \frac{1}{C}\left(I_{iB}^t + I_{eB}^t\right)\Delta t \tag{27}$$

where I_{iB} (I_{eB}) are the sum total ion (electron) current at the external boundary, and C is an equivalent capacitance used to tune ϕ_∞ so that sufficient elec-

14

trons are reflected and the current-free condition holds. The emitted ion current at the thruster outlet (I_{i*}) is assumed constant (Eq. 28), whereas the emitted electron current (I_{e*}) is varied according to Eq. 29 to ensure quasi-neutrality [31]

$$I_{i*} = \frac{q}{m_i}\dot{m}_{i*} \tag{28}$$

$$I_{e*}^{t+1} = K\frac{n_{i0}^t}{n_{e0}^t}I_{e*}^t \tag{29}$$

where $\dot{m}_{i*}$ is the ion mass flow rate at the thruster outlet (predicted by 3D-VIRTUS), K is a positive control constant, and n_{i0} (n_{e0}) are the ion (electron) density at the thruster outlet. Both ions and electrons are injected with the assumption that the plasma flow is aligned with the velocity map predicted by 3D-VIRTUS. It is noted that the model maintains the ability to apply a generic beam divergence angular distribution [31]. The forward-marching ion, electron and neutral distribution functions are taken to be Maxwellian for continuity with the formulation of the fluid model [16]. It is important to consider that the final net electron current (I_{e0}) depends on the number of electrons returned to the thruster outlet, which is driven by the value of ϕ_∞ and the consequent backward-marching electron distribution that is computed and not assumed [30]. In this way, the control strategy implemented couples the plasma potential solution to the net beam current and allows one to compute self-consistently the total potential drop across the plume (namely $|\phi_\infty|$).

The thrust is computed according to Eq. 30 [26]

$$F = \int \sum_I \left(m_I n_I v_{Iz} + p_I\hat{\mathbf{z}}\cdot\hat{\mathbf{k}}\right)dS_B \tag{30}$$

where S_B is the external boundary surface and $\hat{\mathbf{z}}$ the unit vector aligned with the axis of the thruster.

Finally, according to the typical PIC stability criteria [48], the mesh spacing (Δx) satisfies $\Delta x < \gamma\lambda_D$, where $\lambda_D = \sqrt{\epsilon_0 k_B T_e/q^2 n_e}$ is the local Debye length. The factor $\gamma > 1$ is a scaling factor that increases the vacuum permittivity $\tilde{\epsilon}_0 = \gamma^2\epsilon_0$, so as to reduce the computational demand [43]. Likewise, the time-step must satisfy $\Delta t = min(\Delta\tilde{t}_{pe}, \Delta t_{ce}, \Delta t_{CFL})$ where $\Delta\tilde{t}_{pe} =$

15

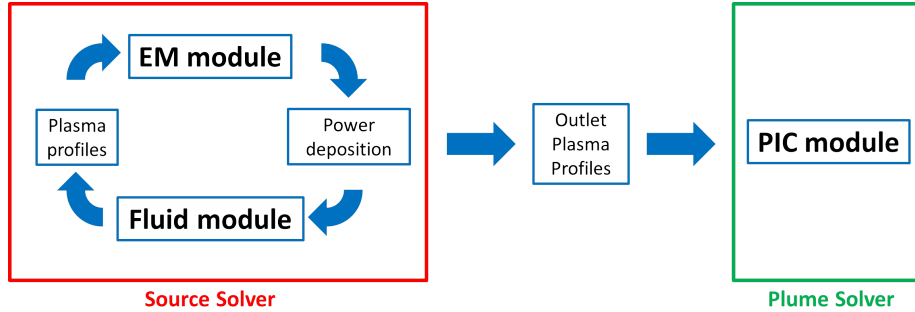Figure 2: Schematic of the 2D thruster simulation tool. The Source solver (3D-VIRTUS) and the Plume solver (Starfish) run sequentially.

$0.1\tilde{\omega}_{pe}{}^{-1}$, $\Delta t_{ce} = 0.35\omega_{ce}^{-1}$, and $\Delta t_{CFL} = 0.5\Delta x/u_e$ are the time-steps required to resolve the scaled plasma frequency, electron gyro-frequency, and electron Courant–Friedrichs–Lewy condition respectively [30]. $\tilde{\omega}_{pe} = \sqrt{q^2 n_e/\tilde{\epsilon}_0 m_e}$ is the scaled plasma frequency.

2.4. Source/Plume Interface

The coupling strategy between the production stage (i.e., 3D-VIRTUS) and the acceleration stage (i.e., Starfish) is schematically depicted in Fig. 2. First, the source solver provides plasma profiles at the thruster outlet, assuming a sonic condition for this boundary. Second, the plume solver takes these profiles as an input and propagates the solution of the plasma expansion.

Specifically, at the interface between the two solvers (i.e., at the truster outlet) the plasma potential is assumed equal to $\phi_0 = 0$. This is a reference value that guarantees consistency between the two solvers, at least in terms of plasma potential maps. In spite of this assumption, the current-free condition is ensured in both the plume and the plasma source since: (i) the total potential drop across the plume $|\phi_\infty|$ is self-consistently computed to ensure a zero net-current leaving the thruster [30], and (ii) according to the imposed boundary conditions, the plasma potential in the source evolves in order to guarantee a zero net-current on each point of the walls.

The most critical aspect related to the proposed interfacing strategy is that,

16
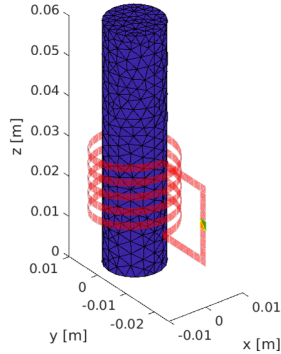
Figure 3: Schematic of the EM setup of the thruster: plasma source and RF antenna.

at the thruster outlet, there is an inconsistency between the fluid and the PIC solvers in terms of particle distribution functions; this will be further discussed in Section 5.4. In fact, in the PIC solver, only the distribution function of the forward-marching particles can be assumed according to the fluid solver. The backward-marching part of the distribution function is computed self-consistently with the total potential drop across the plume $|\phi_\infty|$ and so presents a depleted high-energy tail [49]. As a result, the fluid and the PIC codes might present discontinuity at the thruster outlet in terms of density, temperature and energy fluxes. In Section 5.4 it will be proven that, for the case at hand, using the fluid and the PIC codes in sequence produces a relatively mild error ($\approx 7\%$) on the estimated thrust.

3. Setup

The thruster analysed in this work is a low power - 50 W range - HPT (see schematics in Fig. 1 and Fig. 3, along with an image in Fig. 4). The system has a cylindrical envelope of diameter 0.05 m and length 0.08 m, with a total mass of 0.4 kg. The plasma source is realised in hexagonal boron nitride (hBN), with a cylindrical shape of length $L = 0.060$ m and diameter $D = 0.014$ m. The magnetic field is generated by two rings of Samarium Cobalt (Sm_2Co_{17})

17
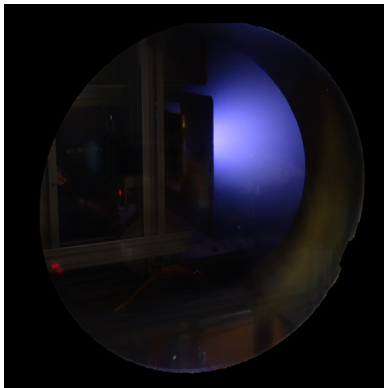
Figure 4: Picture of the HPT under test.

Table 2: Summary of the experimental campaign.

Parameter	Type	Imposed value	Measurement technique
$\dot{m}_0$	Input	0.15 mg/s	Mass flow controller
Pw	Input	$10 - 70$ W	RF probes
T	Output	-	Thrust stand
I_{sp}	Output	-	Thrust stand

permanent magnets (see Fig. 1). At the thruster outlet, the intensity of the magnetic field on the axis is $B_0 = 600$ G. The antenna is a five-turn copper coil with dimensions of length $L_A = 0.020$ m, diameter $D_A = 0.020$ m, and a wire width $w_A = 0.002$ m (see Fig. 3). The structure in which the magnets are encased, along with the casing of the thruster, is polyether ether ketone (PEEK).

The thruster performance has been measured at the high vacuum facility of the University of Padova, where the thruster has been tested inside a cylindrical vacuum chamber with length 2 m and inner diameter 0.6 m. The pumping system has a capacity of 20000 l/s of N_2 [7]. The base pressure in the vacuum chamber with (without) the thruster operating is about 10^{-5} mbar (10^{-6} mbar), while the pressure inside the discharge chamber is in the range of 10^{-2}-10^{-3} mbar.

The RF power was provided to the thruster at a frequency of 2 MHz by means of a water-cooled ENI OEM-12B3-02 linear amplifier driven by a HP 8648A signal generator. A MKS 1179A mass flow controller, whose accuracy is ± 0.01 mg/s, was employed to regulate the propellant flow injected into the discharge chamber [7]. The equipment employed for the characterisation includes a thrust balance, specifically designed for RF thrusters of small-to-medium size [50], and RF probes for vector voltage and current measurement [7]. The former determines the thrust and specific impulse with an uncertainty of 10%–20%; the latter allows the net power provided by the amplifier to be monitored with an uncertainty of 5%.

The propulsive performance was evaluated in terms of thrust (T) and specific impulse (I_{sp}) according to the measures provided by the thrust stand. The thruster was operated with a fixed mass flow rate of xenon $\dot{m}_0 = 0.15$ mg/s. The power provided to the antenna (Pw) was varied from 10 to 70 W. An antenna efficiency of $\eta_A = 0.8$ has been estimated, so the power actually coupled to the plasma is assumed equal to $P_{RF} = \eta_A Pw$. In Table 2, the main input/output parameters of the experimental campaign are summarised.

4. Global Model

In Fig. 5, the results provided by the Global Model, in terms of propulsive performance (i.e., thrust and specific impulse), are compared against experiments. Due to the assumptions made in the Global Model, an uncertainty band of $\pm 20\%$ is attributed to the numerical results. This uncertainty is mainly associated to the assumptions on the plasma profiles (Eqs. 5,6), interactions between the plasma and the walls (Eqs. 8,9), cross sections of the plasma reactions (Table 1), and detachment criterion (Eq. 11) [27, 28]. The propulsive performance (both in terms of T and I_{sp}) increases linearly with the input power Pw. Similar trends are obtained for T and I_{sp} since a constant mass flow rate is imposed (see Table 2). The increment of the propulsive performance with the input power is due to the increased plasma density and electron temperature achievable within
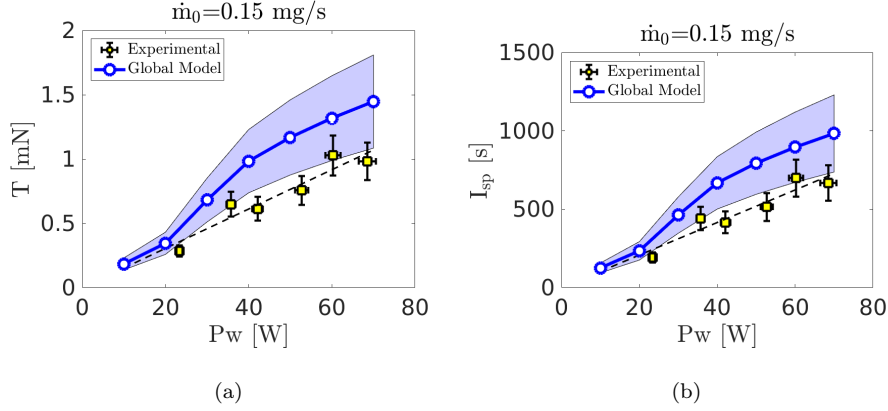
19

Figure 5: Performance predicted with the Global Model compared against measures. (a) Thrust (T), and (b) specific impulse (I_{sp}) in function of the input power (Pw). Mass flow rate $\dot{m}_0 = 0.15$ mg/s

.

the plasma source (see Eq. 11). The latter relation has been thoroughly investi-
gated in [7, 28]. Trends predicted numerically and evaluated experimentally are in good agreement. Moreover, numerical and experimental uncertainty bands overlap. This result can be considered sufficiently accurate for the scope of the Global Model, which is a tool aimed at preliminary characterisation of a cathodeless plasma thruster.

5. 2D Thruster Simulation

A 2D simulation of the overall plasma thruster has been completed for an input power $Pw = 55$ W and a mass flow rate of $\dot{m}_0 = 0.15$ mg/s.

5.1. Source

The results of the fluid module in 3D-VIRTUS are depicted in Fig. 6. The power deposition profile is consistent with an inductive power coupling mode [51, 52], namely the peak is below the antenna and located at the outer radius of the source. Axially, the maximum plasma density occurs at the power deposition peak where, in turn, the intensity of the magnetic field is maximum (up to
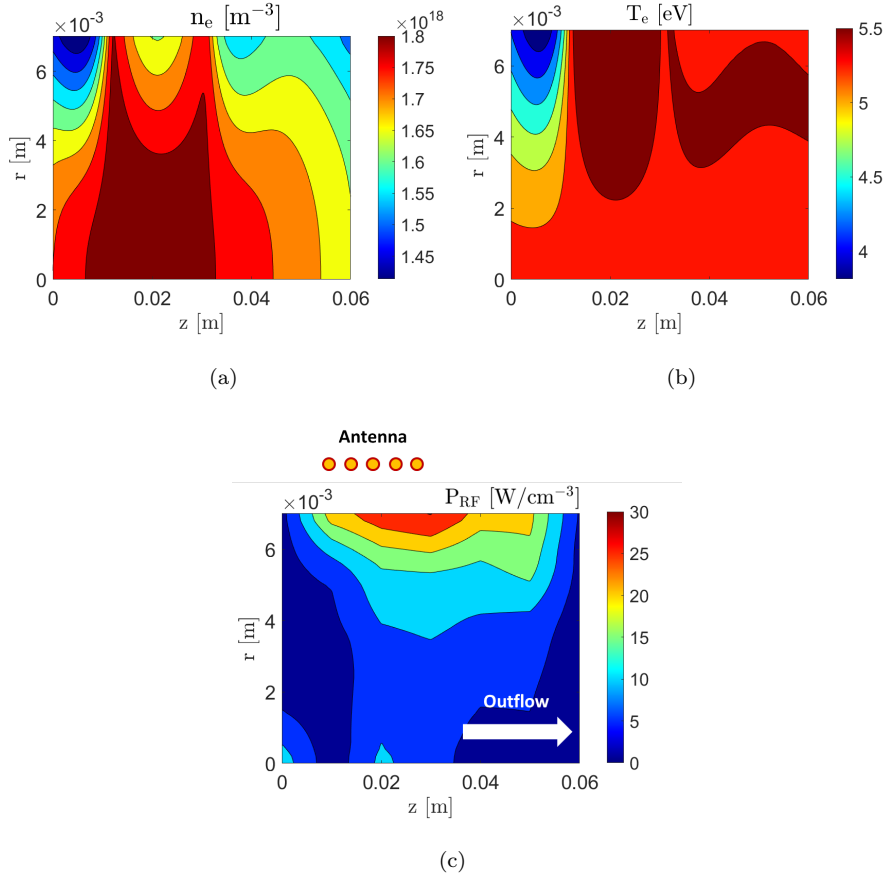
Figure 6: (a) Power coupled to the plasma (P_{RF}), (b) electron density (n_e), and (c) electron temperature (T_e) in function of the radial and axial positions ($r - z$) within the source. Input power $Pw = 55$ W and mass flow rate $\dot{m}_0 = 0.15$ mg/s.

1500 G). The electron density profile follows the magnetic field lines, since dif-
fusion coefficients are reduced up to three orders of magnitude in the direction
perpendicular to the magnetostatic field [29]. Electron temperature is maximum
where magnetic field lines are aligned along the axis of the thruster, as well as
near the outer radius of the discharge; in this position the power deposition is
maximum. Results are qualitatively consistent with measurements performed
on HPTs [53].
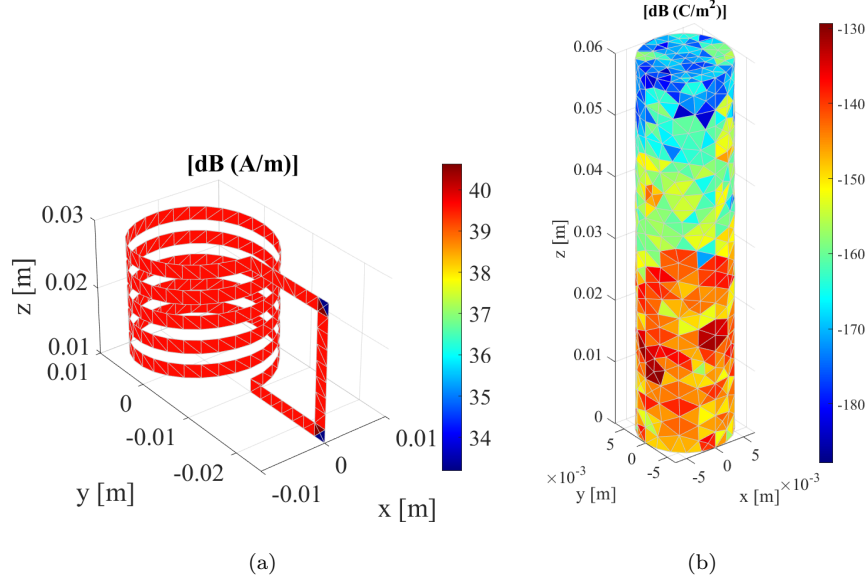
Figure 7: Results of the EM module. (a) Antenna current density J_A, and (b) displacement electric field D_p. Input power $Pw = 55$ W.

5.2. Antenna

The results of the EM module in 3D-VIRTUS are reported in Fig. 7. From the current density profile (J_A), it is possible to compute the antenna impedance [13], the value of which is $Z \approx 10 + j100$ Ω, where j is the imaginary unit. The displacement electric field map in the plasma (D_p) is used to derive the power deposition profile depicted in Fig. 6(c) [16]. For further details on the computational mesh used in the EM module, refer to the Appendix.

5.3. Plume

The plasma profiles throughout the thruster are reported in Fig. 8. Starfish has been used for handling the acceleration stage, namely the portion of the domain downstream of the thruster outlet. The plasma expansion is driven by the geometry of the magnetostatic field [30]. The electron density decreases rapidly (more than four orders of magnitude) across the outermost field line that intercepts the edge of the thruster outlet. The thruster case is in contact

22
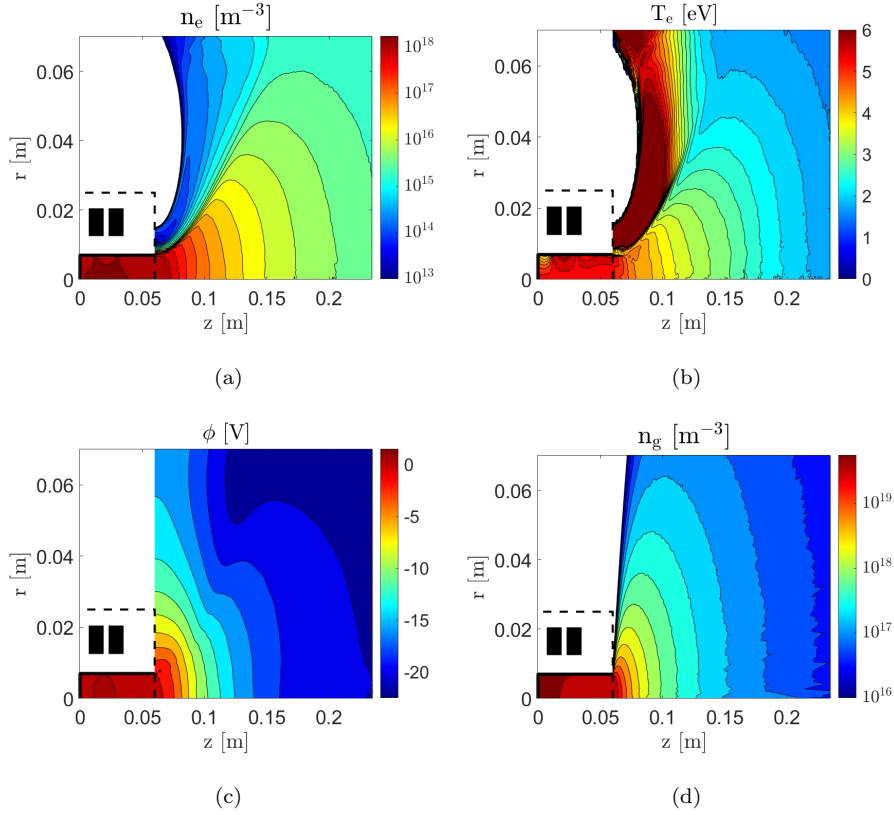
Figure 8: (a) Electron density (n_e), (b) electron temperature (T_e), (c) plasma potential (ϕ), and (d) neutral density (n_g) in function of the radial and the axial positions ($r - z$) within the overall thruster. Input power $Pw = 55$ W and mass flow rate $\dot{m}_0 = 0.15$ mg/s.

360   with a very low density population ($n_e \approx 10^{13}$ m^{-3}) of energetic electrons ($T_e > 6$ eV). These particles are the few with enough energy to escape the magnetic confinement [30]. Being that the axial cross section of the plume progressively increases, the decrement in the electron density is a consequence of the mass conservation law [30]. The electron cooling can be described with a

365   piece-wise polytropic expansion law [30].

The plasma potential is equal to ϕ_0 at the thruster outlet, consistent with the interfacing strategy (see Section 2). The potential drop across the magnetic nozzle is calculated self-consistently according to the methodology prescribed in
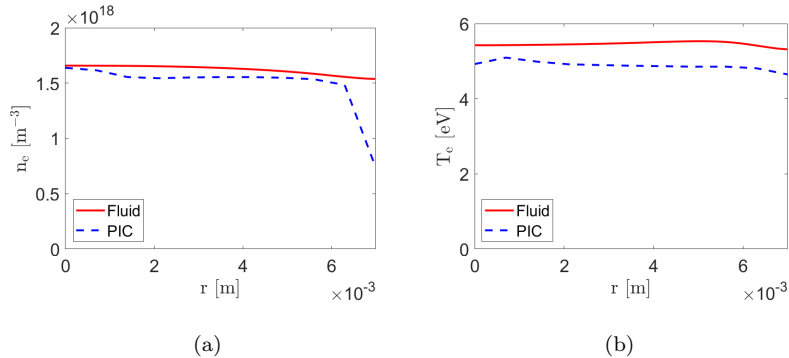
23

Figure 9: (a) Electron density (n_e), and (b) electron temperature (T_e) in function of the radial position (r) at the thruster outlet. Predictions from the source solver (Fluid) and the plume solver (PIC) are compared. Input power $Pw = 55$ W and mass flow rate $\dot{m}_0 = 0.15$ mg/s.

Section 2. The result, $\phi_\infty \approx -33$ V, is in agreement with the simplified model reported in [3] for a xenon plasma with $T_e \approx 5.5$ eV. The neutral plasma density profile is consistent with a free molecular expansion [54].

5.4. Source/Plume Interface

In Fig. 9 the radial electron density and temperature profiles at the thruster outlet are shown. The values provided by the fluid and the PIC codes (i.e., the solutions of the production and the acceleration stages respectively) present non-negligible discontinuities, up to 30%. This is associated to the control loop implemented in the PIC model. As mentioned previously, at the thruster outlet, only properties associated to the forward-marching electrons can be imposed (i.e., I_{e*}). The final plasma profiles from the PIC simulation in Fig. 9 are obtained by integrating the distribution function of the electrons which includes also the backward-marching population [55]. The dynamics of the latter is a result of the simulation being strongly dependent on ϕ_∞ [31], not a value that can be known *a priori*. As a result, the output of the PIC code presents inconsistencies with respect to the input provided by the fluid solver. Indeed, the value of T_e given by the fluid model is that of a full Maxwellian distribution function (see Section 2.2) whereas, in the PIC, the decrement in its value represents the

24

high-energy population of free electrons that escaped the potential drop of the plume. This causes a depletion of the backward-marching high-energy tail of the distribution function [49]. Importantly, this inconsistency is not affected by the assumed forward-marching distribution function (that might be non-Maxwellian both in the fluid and the PIC solvers [34]) but only to the computed, and not assumed, backward-marching PIC solution. It is possible to quantify the effect of this continuity error on the estimates of propulsive performance by considering the net power at the magnetic nozzle throat which, according to the PIC solver, reads [42]

$$P_{ex} = \left\langle \frac{1}{\Delta t} \sum_I \left(\sum_{ejected} \frac{1}{2} m_I v_I^2 - \sum_{absorbed} \frac{1}{2} m_I v_I^2 \right) \right\rangle_t \tag{31}$$

where the summation is performed over the particles of species I ($I = e$, i, 0) that are ejected (absorbed) through the thruster outlet at each time-step. Angular brackets represent a value averaged over multiple time-steps (in the order of 10^4) to minimise numerical noise. According to the energy equation (Eq. 16), the fluid model yields a nozzle power of $P_{ex} = 3.48$ W. With Eq. 31, the PIC model gives $P_{ex} = 3.16$ W, a 7% loss. Since the thrust is expected to scale linearly with power (see Fig.10), an underestimate of propulsive performance of the same magnitude can be expected. Finally, the results presented in Section 5.5 confirm that this issue has a minor effect on the estimation of the propulsive performance, since the disagreement between experiments and simulations is below 20%.

5.5. Propulsive Performance

The estimation of the propulsive performance obtained with the 2D simulation of the HPT has been reported in Fig. 10. Specifically, thrust has been computed by coupling the solution of the production stage with both the semi-analytical formulation implemented in the Global Model (i.e., Eqs. 11,12,13) and the results provided by the Starfish PIC model (i.e., Eq. 30). In both cases, the estimation of the propulsive performance matches better the experimental benchmark with respect to only the Global Model. The most accurate result
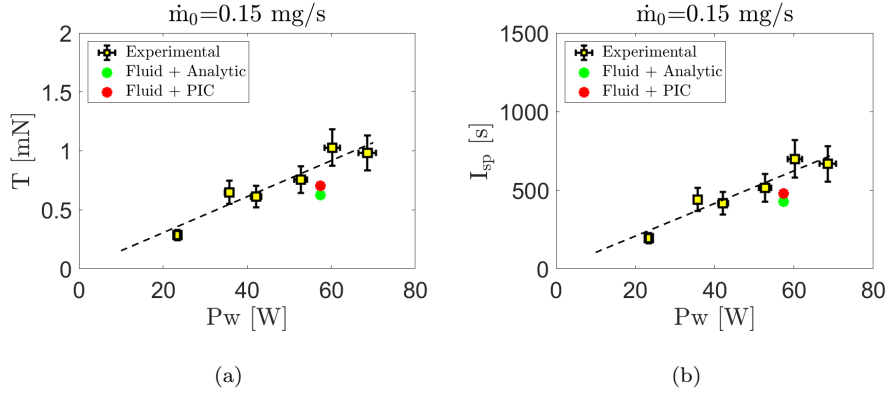
25

Figure 10: Performance predicted numerically compared against measures. (a) Thrust (T), and (b) specific impulse (I_{sp}) in function of the input power (Pw). Mass flow rate $\dot{m}_0 = 0.15$ mg/s.

is provided by coupling 3D-VIRTUS and Starfish, where the difference between numerical and experimental results is less than 20%.

6. 3D Plume Simulation

3D fully kinetic PIC simulations have been performed with the open-source code SPIS. This tool has been modified according to the methodology described in Section 2.3 [31]. SPIS simulates the dynamics of a magnetised plasma plume in a non-axisymmetric (x, y, z) domain. It has therefore been used to evaluate the mutual interactions between the propulsion system plume, the spacecraft surfaces, and the environmental plasma. The outputs discussed in the following are the mutual influence of the environmental plasma and the plume, the flux of particles impinging on the thruster case, and the electron trajectories.

The simulation domain is a cylinder of height 3 m and radius 1.5 m, centred on the thruster outlet. The spacecraft has dimensions $H_c = 0.8$ m, $L_c = 0.8$ m, $W_c = 0.2$ m (see Fig. 11). The thruster considered is consistent with that described in Section 3, with input power $Pw = 55$ W and mass flow rate $\dot{m}_0 = 0.15$ mg/s. The orbital altitude is 600 km, therefore the environmental plasma is assumed to be composed of only electrons and oxygen ions (O^+). At
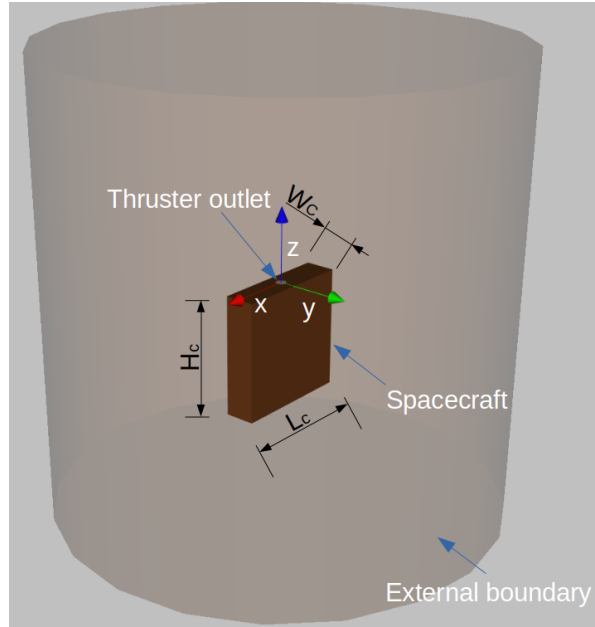
26

Figure 11: Scheme of the numerical setup adopted for the 3D PIC simulations.

this altitude, the O^+ density is approximately 10^{11} m^{-3} [56]. The spacecraft velocity V_{SC} is 7.5 km/s. The orientation of the spacecraft with respect to the velocity vector has been reversed in order to evaluate the mutual influence between the propulsion system plume and environmental plasma.

The first analysis aims to evaluate how the thruster affects the trajectories of the environmental plasma particles and, in turn, the contamination of the spacecraft surfaces due to atomic oxygen. Fig. 12 depicts the speed of O^+ ions (v_{O+}) in the case of $\mathbf{V}_{SC} = (0, 0, V_{SC})$ and $\mathbf{V}_{SC} = (0, 0, -V_{SC})$ respectively. Due to the low plasma density, collisions between environment plasma and the plume are negligible [57]. Therefore, the behaviour of the environmental plasma is almost completely determined by the potential field associated to the plasma plume. The trajectories of O^+ particles are strongly deflected near the thruster outlet, where the plasma potential peaks of more than 30 V with respect to ϕ_∞ (see Fig. 8(c)).

Fig. 13 depicts the density and the speed of Xe^+ ions for $\mathbf{V}_{SC} = (0, 0, V_{SC})$

27

and $\mathbf{V}_{SC} = (0, 0, -V_{SC})$ respectively. The plume is near-unaffected by the environmental plasma since the density of Xe$^+$ particles is several orders of
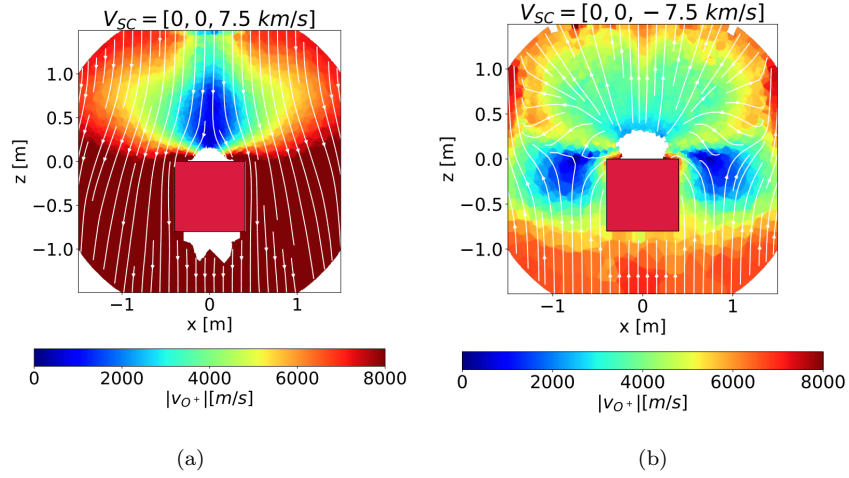

Figure 12: Speed of the O$^+$ particles (v_{O+}) in the $x - z$ plane. The two cases compared are (a) $\mathbf{V}_{SC} = (0, 0, V_{SC})$, and (b) $\mathbf{V}_{SC} = (0, 0, -V_{SC})$. Input power $Pw = 55$ W and mass flow rate $\dot{m}_0 = 0.15$ mg/s.
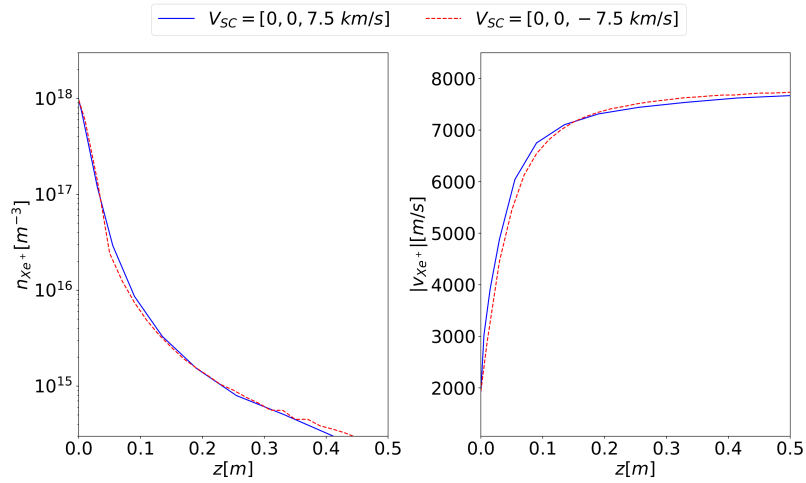

Figure 13: Density n_{Xe+} (left) and speed v_{Xe+} (right) of Xe$^+$ particles in function of the axial position z. The two cases compared are $\mathbf{V}_{SC} = (0, 0, V_{SC})$ (solid line), and $\mathbf{V}_{SC} = (0, 0, -V_{SC})$ (dashed line). Input power $Pw = 55$ W and mass flow rate $\dot{m}_0 = 0.15$ mg/s.
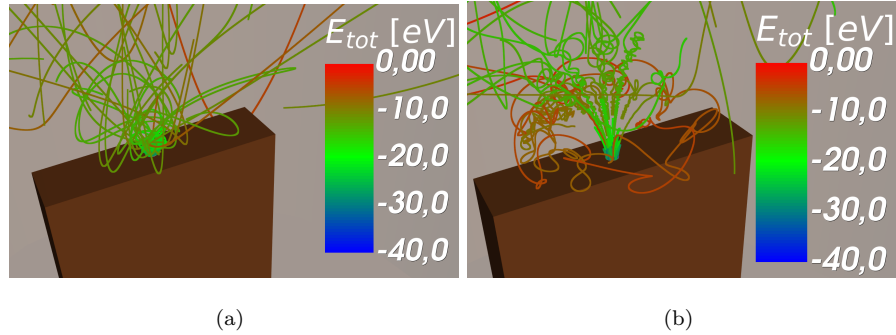
Figure 14: Electron trajectories in case of (a) non-magnetized plume, (b) magnetized plume. Colour bar refers to the total energy of each particle E_{tot}. Input power $Pw = 55$ W and mass flow rate $\dot{m}_0 = 0.15$ mg/s.

magnitude larger than the density of O^+.

450   Finally, a comparison has been conducted between the magnetised case, where the field depicted in Fig. 1 has been assumed, and a non-magnetised case (i.e., $B_0 = 0$ G). In the magnetised case, only 1.6% of the emitted particles impinge on the thruster case; this value increases up to 17% without the magnetic field. This is consistent with the results presented in Section 5.3 that show a

455 strong confinement imposed by the presence of the magnetic nozzle. In Fig. 14, electron trajectories are depicted; the colour map refers to the total energy (E_{tot}) of each particle. In the non-magnetised case, electrons describe chaotic trajectories consistent with the assumption of a Maxwellian distribution function at the thruster outlet. In the magnetised case, particles in the proximity

460 of the thruster outlet, namely where the intensity of the magnetostatic field is higher, are frozen to the field lines and describe the expected gyro-motion [58]. Further downstream, electrons lose their magnetisation and describe a random motion. Future studies on the trajectories of the electrons will be conducted to investigate their relationship with the detachment phenomenon [3].

7. Conclusions

A numerical suite capable of simulating the propulsive performance and the plasma dynamics in a cathodeless plasma thruster has been presented. It consists of a Global Model [27, 28] for the preliminary estimate of propulsive performance, the 3D-VIRTUS [16] code for plasma transport in the production
470 stage, along with Starfish [30] and SPIS [31] for the solution of the acceleration stage. The results of the Global Model, and of the coupled 3D-VIRTUS/Starfish, have been benchmarked against measurements of the propulsive performance (i.e., thrust and specific impulse). The agreement between experiments and the Global Model is consistently better than 50%, and differences reduce to 20%
475 with a 2D simulation approach.

In future works, the interfacing strategy between 3D-VIRTUS and Starfish will be improved to solve the inconsistencies on the interface boundary. This will involve running the fluid and the PIC solvers iteratively. The backward-marching electron distribution from the PIC will therefore feedback to the fluid
480 model, and reciprocal particles and energy fluxes at the interface will be defined. Both 3D-VIRTUS and the Global Model will be improved to handle generic distribution functions. To date, this capability has been implemented in terms of plasma reactions [27], but not yet for diffusion coefficients. The SPIS code will be used to investigate the relationship between the demagnetisation of the
485 electrons and the detachment phenomenon [3].

Finally, it is worth noting that the numerical suite presented in this work can also simulate the plasma dynamics in applications other than electric propulsion, such as plasma antennas [59, 60, 61, 62, 63, 64] and water treatment reactors [65].

Appendix. Numerical Sensitivity

490 A sensitivity analysis on two aspects of the numerical simulations is reported in the following: (i) definition of the boundary condition for the ion continuity equation, and (ii) mesh resolution for the solution of the EM wave propagation into the plasma.
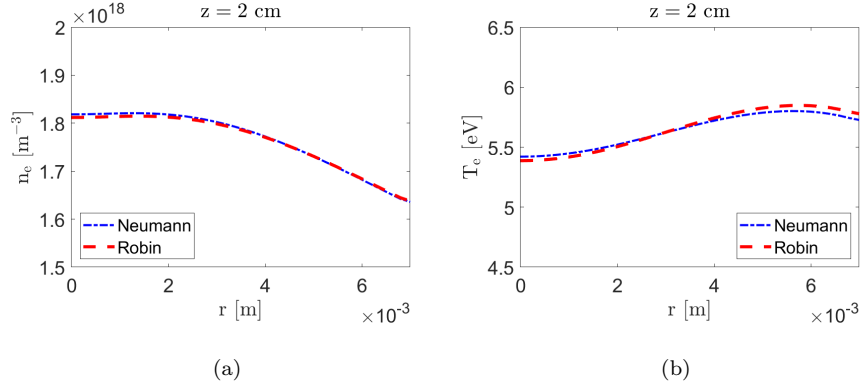
Figure 15: (a) Electron density (n_e), and (b) electron temperature (T_e) in function of the radial position (r) at $z = 2$ cm. Comparison between Neumann and Robin boundary conditions for the ions continuity. Input power $Pw = 55$ W and mass flow rate $\dot{m}_0 = 0.15$ mg/s.

Ion Boundary Conditions

Results presented in Section 5.1 are obtained assuming a zero-gradient Neumann type boundary condition for the ion continuity. More often, a Robin type boundary condition is imposed according to [66]

$$\mathbf{\Gamma}_i \cdot \hat{\mathbf{k}} = \left(\bar{\bar{\mu}}_i \mathbf{E} \cdot \hat{\mathbf{k}} + \frac{1}{2} u_{th} + \mathbf{u}_0 \cdot \hat{\mathbf{k}} \right) n_i \tag{32}$$

where $\hat{\mathbf{k}}$ is a unit vector normal to the boundary. In Fig. 15, results obtained imposing a zero-gradient Neumann and a Robin type boundary condition are compared. The inputs of the fluid module of 3D-VIRTUS are: $Pw = 55$ W and $\dot{m}_0 = 0.15$ mg/s. Radial profiles of electron density (n_e) and electron temperature (T_e) are computed at $z = 2$ cm. The two formulations of the boundary conditions produce differences that are in the order of few percent points. This result can be interpreted by considering that, according to the definition of $\mathbf{\Gamma}_i$ given in Eq. 18, a zero-gradient boundary condition is equivalent to

$$\mathbf{\Gamma}_i \cdot \hat{\mathbf{k}} = \left(\bar{\bar{\mu}}_i \mathbf{E} \cdot \hat{\mathbf{k}} + \mathbf{u}_0 \cdot \hat{\mathbf{k}} \right) n_i \tag{33}$$

In the case at hand, $u_{th} \ll \bar{\bar{\mu}}_i \mathbf{E} \cdot \hat{\mathbf{k}}$ (a couple of orders of magnitude difference), namely the fluxes prescribed in Eq. 32 and Eq. 33 are almost identical.
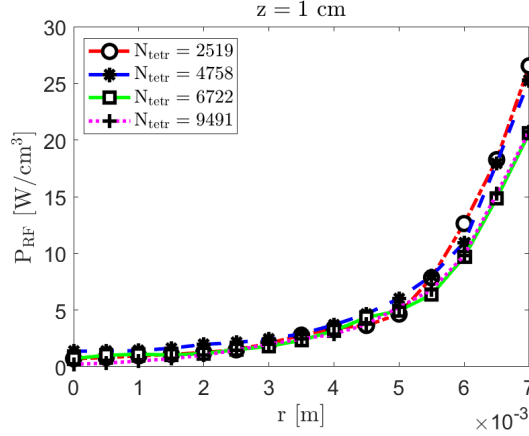
31

Figure 16: Power coupled to the plasma (P_{RF}) in function of the radial position (r) at $z = 1$ cm. Comparison between different numbers of tetrahedra N_{tetr} that mesh the plasma volume. Input power $Pw = 55$ W.

Table 3: Computation time of the EM module in function of the number of tetrahedra (N_{tetr}) that mesh the plasma volume.

N_{tetr} [#]	2519	4758	6722	9491
time [h]	0.55	1.82	3.72	7.81

EM module mesh

The EM module of 3D-VIRTUS relies on a 3D unstructured mesh to solve the wave propagation within the plasma. The number of tetrahedra that constitute the grid (N_{tetr}) is critical in terms of the estimated power deposition profile and, in turn, of predicted propulsive performance [14, 16]. In Fig.16, the results of a sensitivity analysis performed on N_{tetr} are depicted. The radial profile of the power coupled to the plasma (P_{RF}) is given at $z = 1$ cm. If $N_{tetr} > 6000$, the power deposition profile is not significantly (more than 5%) influenced by N_{tetr}. The value $N_{tetr} = 6722$ represents a trade off between accuracy and minimisation of the computational time (see Table 3). The results presented in Section 5 are obtained with this value of N_{tetr}.

32

References

[1] S. Mazouffre, Electric propulsion for satellites and spacecraft: established technologies and novel approaches, Plasma Sources Science and Technology 25 (3) (2016) 033002.

[2] D. M. Goebel, I. Katz, Fundamentals of electric propulsion: ion and Hall thrusters, Vol. 1, John Wiley & Sons, 2008.

[3] K. Takahashi, Helicon-type radiofrequency plasma thrusters and magnetic plasma nozzles, Reviews of Modern Plasma Physics 3 (1) (2019) 1–61.

[4] M. Manente, F. Trezzolani, M. Magarotto, E. Fantino, A. Selmo, N. Bellomo, E. Toson, D. Pavarin, Regulus: A propulsion platform to boost small satellite missions, Acta Astronautica 157 (2019) 241–249.

[5] F. Cannat, T. Lafleur, J. Jarrige, P. Chabert, P.-Q. Elias, D. Packan, Optimization of a coaxial electron cyclotron resonance plasma thruster with an analytical model, Physics of Plasmas 22 (5) (2015) 053503.

[6] D. Arnush, F. F. Chen, Generalized theory of Helicon waves. II. Excitation and absorption, Physics of Plasmas 5 (5) (1998) 1239–1254.

[7] M. Magarotto, M. Manente, F. Trezzolani, D. Pavarin, Numerical model of a Helicon plasma thruster, IEEE Transactions on Plasma Science 48 (4) (2020) 835–844.

[8] M. Magarotto, D. Melazzi, D. Pavarin, Study on the influence of the magnetic field geometry on the power deposition in a Helicon plasma source, Journal of Plasma Physics 85 (4) (2019) 905850404.

[9] E. Ahedo, M. Merino, Two-dimensional supersonic plasma acceleration in a magnetic nozzle, Physics of Plasmas 17 (7) (2010) 073501.

[10] N. Bellomo, et al., Design and in-orbit demonstration of Regulus, an iodine electric propulsion system, CEAS Space Journal 14 (2022) 79–90.

33

[11] N. Bellomo, et al., Enhancement of microsatellites' mission capabilities: Integration of Regulus electric propulsion module into UniSat-7, in: Proceedings of the 70th International Astronautical Congress (IAC), IAC-19,C4,8-B4.5A,5, Washington, DC, USA, 2019.

[12] A. V. Arefiev, B. N. Breizman, Theoretical components of the VASIMR plasma propulsion concept, Physics of Plasmas 11 (5) (2004) 2942–2949.

[13] K. Takahashi, Magnetic nozzle radiofrequency plasma thruster approaching twenty percent thruster efficiency, Scientific reports 11 (2021) 2768.

[14] D. Melazzi, V. Lancellotti, ADAMANT: A surface and volume integral-equation solver for the analysis and design of Helicon plasma sources, Computer Physics Communications 185 (7) (2014) 1914–1925.

[15] J. Zhou, D. Pérez-Grande, P. Fajardo, E. Ahedo, Numerical treatment of a magnetized electron fluid model within an electromagnetic plasma thruster simulation code, Plasma Sources Science and Technology 28 (11) (2019) 115004.

[16] M. Magarotto, D. Melazzi, D. Pavarin, 3D-VIRTUS: Equilibrium condition solver of radio-frequency magnetized plasma discharges for space applications, Computer Physics Communications 247 (2020) 106953.

[17] A. V. Arefiev, B. N. Breizman, Magnetohydrodynamic scenario of plasma detachment in a magnetic nozzle, Physics of Plasmas 12 (4) (2005) 043504.

[18] G. Sánchez-Arriaga, J. Zhou, E. Ahedo, M. Martínez-Sánchez, J. J. Ramos, Kinetic features and non-stationary electron trapping in paraxial magnetic nozzles, Plasma Sources Science and Technology 27 (3) (2018) 035002.

[19] F. Cichocki, A. Domínguez-Vázquez, M. Merino, E. Ahedo, Hybrid 3D model for the interaction of plasma thruster plumes with nearby objects, Plasma Sources Science and Technology 26 (12) (2017) 125008.

[20] T. Lafleur, Helicon plasma thruster discharge model, Physics of Plasmas 21 (4) (2014) 043507.

[21] E. Ahedo, J. Navarro-Cavallé, Helicon thruster plasma modeling: Two-dimensional fluid-dynamics and propulsive performances, Physics of Plasmas 20 (4) (2013) 043512.

[22] A. Fruchtman, K. Takahashi, C. Charles, R. Boswell, A magnetic nozzle calculation of the force on a plasma, Physics of Plasmas 19 (3) (2012) 033507.

[23] M. Magarotto, D. Pavarin, Parametric study of a cathode-less radio frequency thruster, IEEE Transactions on Plasma Science 48 (8) (2020) 2723–2735.

[24] E. Ahedo, S. Correyero, J. Navarro-Cavallé, M. Merino, Macroscopic and parametric study of a kinetic plasma expansion in a paraxial magnetic nozzle, Plasma Sources Science and Technology 29 (4) (2020) 045017.

[25] M. Li, M. Merino, E. Ahedo, H. Tang, On electron boundary conditions in PIC plasma thruster plume simulations, Plasma Sources Science and Technology 28 (3) (2019) 034004.

[26] Á. Sánchez-Villar, J. Zhou, E. Ahedo, M. Merino, Coupled plasma transport and electromagnetic wave simulation of an ECR thruster, Plasma Sources Science and Technology 30 (4) (2021) 045005.

[27] N. Souhair, M. Magarotto, E. Majorana, F. Ponti, D. Pavarin, Development of a lumping methodology for the analysis of the excited states in plasma discharges operated with argon, neon, krypton, and xenon, Physics of Plasmas 28 (9) (2021) 093504.

[28] M. Guaita, M. Magarotto, M. Manente, D. Pavarin, M. Lavagna, Semi-analytical model of a Helicon plasma thruster, IEEE Transactions on Plasma Science 50 (2) (2022) 425–438.

35

[29] N. Souhair, M. Magarotto, F. Ponti, D. Pavarin, Analysis of the plasma transport in numerical simulations of Helicon plasma thrusters, AIP Advances 11 (11) (2021) 115016.

[30] S. Andrews, S. Di Fede, M. Magarotto, Fully kinetic model of plasma expansion in a magnetic nozzle, Plasma Sources Science and Technology 31 (2022) 035022.

[31] S. Di Fede, M. Magarotto, S. Andrews, D. Pavarin, Simulation of the plume of a magnetically enhanced plasma thruster with SPIS, Journal of Plasma Physics 87 (6) (2021) 905870611.

[32] P. Chabert, J. Arancibia Monreal, J. Bredin, L. Popelier, A. Aanesland, Global model of a gridded-ion thruster powered by a radiofrequency inductive coil, Physics of Plasmas 19 (7) (2012) 073512.

[33] M. A. Lieberman, A. J. Lichtenberg, Principles of plasma discharges and materials processing, John Wiley & Sons, 2005.

[34] M. Merino, E. Ahedo, Two-dimensional quasi-double-layers in two-electron-temperature, current-free plasmas, Physics of Plasmas 20 (2) (2013) 023502.

[35] F. F. Chen, D. D. Blackwell, Upper limit to landau damping in helicon discharges, Physical review letters 82 (13) (1999) 2677.

[36] J. Kline, E. Scime, Parametric decay instabilities in the helix helicon plasma source, Physics of Plasmas 10 (1) (2003) 135–144.

[37] S. Hepner, B. Wachs, B. Jorns, Wave-driven non-classical electron transport in a low temperature magnetically expanding plasma, Applied Physics Letters 116 (26) (2020) 263502.

[38] J. Boeuf, L. Garrigues, Low frequency oscillations in a stationary plasma thruster, Journal of Applied Physics 84 (7) (1998) 3541–3554.

[39] J. Zhou, A. Domínguez-Vázquez, P. Fajardo, E. Ahedo, Magnetized fluid electron model within a two-dimensional hybrid simulation code for electrodeless plasma thrusters, Plasma Sources Science and Technology.

[40] G. Gallina, M. Magarotto, M. Manente, D. Pavarin, Enhanced bidimensional pic: an electrostatic/magnetostatic particle-in-cell code for plasma based systems, Journal of Plasma Physics 85 (2) (2019) 905850205.

[41] H. Qin, S. Zhang, J. Xiao, J. Liu, Y. Sun, W. M. Tang, Why is boris algorithm so good?, Physics of Plasmas 20 (8) (2013) 084503.

[42] J. A. Bittencourt, Fundamentals of plasma physics, Springer Science & Business Media, 2004.

[43] J. J. Szabo, Fully kinetic numerical modeling of a plasma thruster, Ph.D. thesis, Massachusetts Institute of Technology (2001).

[44] A. Dalgarno, M. C. McDowell, A. Williams, The mobilities of ions in unlike gases, Philosophical Transactions of the Royal Society of London. Series A, Mathematical and Physical Sciences 250 (982) (1958) 411–425.

[45] D. Rapp, W. E. Francis, Charge exchange between gaseous ions and atoms, The Journal of Chemical Physics 37 (11) (1962) 2631–2645.

[46] K. Koura, H. Matsumoto, Variable soft sphere molecular model for air species, Physics of Fluids A: Fluid Dynamics 4 (5) (1992) 1083–1085.

[47] S. Cho, H. Watanabe, K. Kubota, S. Iihara, K. Fuchigami, K. Uematsu, I. Funaki, Study of electron transport in a hall thruster by axial–radial fully kinetic particle simulation, Physics of Plasmas 22 (10) (2015) 103523.

[48] C. K. Birdsall, A. B. Langdon, Plasma physics via computer simulation, CRC press, 2004.

[49] T. Lafleur, F. Cannat, J. Jarrige, P. Elias, D. Packan, Electron dynamics and ion acceleration in expanding-plasma thrusters, Plasma Sources Science and Technology 24 (6) (2015) 065013.

37

[50] F. Trezzolani, M. Magarotto, M. Manente, D. Pavarin, Development of a counterbalanced pendulum thrust stand for electric propulsion, Measurement 122 (2018) 494–501.

[51] F. Romano, et al., RF helicon-based inductive plasma thruster (IPT) design for an atmosphere-breathing electric propulsion system (ABEP), Acta Astronautica 176 (2020) 476–483.

[52] A. Ellingboe, R. Boswell, Capacitive, inductive and Helicon-wave modes of operation of a Helicon plasma source, Physics of Plasmas 3 (7) (1996) 2797–2804.

[53] A. E. Vinci, S. Mazouffre, Direct experimental comparison of krypton and xenon discharge properties in the magnetic nozzle of a helicon plasma source, Physics of Plasmas 28 (3) (2021) 033504.

[54] P. Molmud, Expansion of a rarefield gas cloud into a vacuum, The Physics of fluids 3 (3) (1960) 362–366.

[55] M. Martinez-Sanchez, J. Navarro-Cavalle, E. Ahedo, Electron cooling and finite potential drop in a magnetized plasma expansion, Physics of Plasmas 22 (5) (2015) 053501.

[56] S. Andrews, L. Berthoud, Characterising satellite aerodynamics in very low earth orbit inclusive of ion thruster plume-thermosphere/ionosphere interactions, Acta Astronautica 170 (2020) 386–396.

[57] S. J. Araki, R. E. Wirz, Ion–neutral collision modeling using classical scattering with spin-orbit free interaction potential, IEEE Transactions on Plasma Science 41 (3) (2013) 470–480.

[58] F. F. Chen, et al., Introduction to plasma physics and controlled fusion, Vol. 1, Springer, 1984.

[59] G. Mansutti, P. De Carlo, M. A. Hannan, F. Boulos, P. Rocca, A.-D. Capobianco, M. Magarotto, A. Tuozzi, Modeling and design of a plasma-

based transmit-array with beam scanning capabilities, Results in Physics 16 (2020) 102923.

[60] A. Daykin-Iliopoulos, F. Bosi, F. Coccaro, M. Magarotto, A. Papadimopoulos, P. De Carlo, C. Dobranszki, I. Golosnoy, S. Gabriel, Characterisation of a thermionic plasma source apparatus for high-density gaseous plasma antenna applications, Plasma Sources Science and Technology 29 (11) (2020) 115002.

[61] M. Magarotto, P. de Carlo, G. Mansutti, F. J. Bosi, N. E. Buris, A.-D. Capobianco, D. Pavarin, Numerical suite for gaseous plasma antennas simulation, IEEE Transactions on Plasma Science 49 (1) (2020) 285–297.

[62] P. De Carlo, M. Magarotto, G. Mansutti, A. Selmo, A.-D. Capobianco, D. Pavarin, Feasibility study of a novel class of plasma antennas for SatCom navigation systems, Acta Astronautica 178 (2021) 846–853.

[63] P. De Carlo, M. Magarotto, G. Mansutti, S. Boscolo, A.-D. Capobianco, D. Pavarin, Experimental characterization of a plasma dipole in the UHF band, IEEE Antennas and Wireless Propagation Letters 20 (9) (2021) 1621–1625.

[64] G. Mansutti, P. De Carlo, M. Magarotto, M. A. Hannan, P. Rocca, A.-D. Capobianco, D. Pavarin, A. Tuozzi, Design of a hybrid metal-plasma transmit-array with beam-scanning capabilities, IEEE Transactions on Plasma Science 50 (3) (2022) 662–669.

[65] M. Saleem, O. Biondo, G. Sretenović, G. Tomei, M. Magarotto, D. Pavarin, E. Marotta, C. Paradisi, Comparative performance assessment of plasma reactors for the treatment of PFOA; reactor design, kinetics, mineralization and energy yield, Chemical Engineering Journal 382 (2020) 123031.

[66] G. Hagelaar, F. De Hoog, G. Kroesen, Boundary conditions in fluid models of gas discharges, Physical Review E 62 (1) (2000) 1452.